



Article

Innovative Mechanical Design Strategy for Actualizing 80 kg-Class X-Band Active SAR Small Satellite of S-STEP

Seong-Cheol Kwon ¹, Ji-Hae Son ¹, Sung-Chan Song ¹, Jin-Han Park ¹, Kyung-Rae Koo ¹ and Hyun-Ung Oh ^{2,*}

- ¹ Satellite System Division, Hanwha System 304 Cheoin-gu, Yongin 449-886, Korea; seongcheol.kwon@hanwha.com (S.-C.K.); sj311228@hanwha.com (J.-H.S.); sungchan.song@hanwha.com (S.-C.S.); jinhhan22.park@hanwha.com (J.-H.P.); kr.koo@hanwha.com (K.-R.K.)
- ² Space Technology Synthesis Laboratory, Department of Smart Vehicle System Engineering, Chosun University, (Agency for Defense Development: Additional Post), 375 Seosuk-dong, Dong-gu, Gwangju 501-759, Korea
- * Correspondence: ohu129@chosun.ac.kr

Abstract: The Small SAR Technology Experimental Project (S-STEP) mission aims to develop a new (space-based 80 kg-class active X-band synthetic aperture radar (SAR)) satellite with a main imaging mode of 1 m resolution stripmap. In the S-STEP mission, to achieve the design goal of developing faster, cheaper, better, and lighter small SAR satellite systems, innovative thermo-mechanical design approaches have been proposed and investigated. The major design approaches are the bus-payload integrated flat plate-type structure, multifunctional transmit/receive (TR) module, and dedicated vibration-free orbit deployer (VFOD) with the function of whole spacecraft vibration isolation. To validate the feasibility of the innovative mechanical design of S-STEP, a structural analysis considering launch and on-orbit environments is performed. In addition, development test results are presented to confirm the effectiveness of the proposed design approach for VFOD.

Keywords: small satellite; synthetic aperture radar (SAR); new space; whole spacecraft vibration isolation



Citation: Kwon, S.-C.; Son, J.-H.; Song, S.-C.; Park, J.-H.; Koo, K.-R.; Oh, H.-U. Innovative Mechanical Design Strategy for Actualizing 80 kg-Class X-Band Active SAR Small Satellite of S-STEP. *Aerospace* **2021**, *8*, 149. <https://doi.org/10.3390/aerospace8060149>

Academic Editor: M. Reza Emami

Received: 8 April 2021

Accepted: 22 May 2021

Published: 26 May 2021

Publisher's Note: MDPI stays neutral with regard to jurisdictional claims in published maps and institutional affiliations.



Copyright: © 2021 by the authors. Licensee MDPI, Basel, Switzerland. This article is an open access article distributed under the terms and conditions of the Creative Commons Attribution (CC BY) license (<https://creativecommons.org/licenses/by/4.0/>).

1. Introduction

The start of a new space paradigm has changed the development philosophy in the space engineering field worldwide. The new space refers to the recent commercialization of the space sector, which is led primarily by private industries rather than government-funded organizations. These industries are driving a better, faster, cheaper, and lighter space development paradigm [1]. There are several expressions in space communication that accelerate the new space era. Examples include an increase in the number of small satellite launches, a more prominent role for small satellites, and larger constellations and improved coordination between small satellites. Among these expressions, one of the major accelerators for the new space paradigm is the emergence of small satellite constellations, providing all types of services over large geographical areas or spanning the entire globe [2]. In addition, the massive production capability of small satellites based on the standardized satellite platform, commercial grade on-board hardware, and multiple small satellites launched by using a ride-share program make the small satellite platform an attractive approach to realize various challenging missions that require high system temporal performance, such as synthetic aperture radar (SAR) imaging, real-time remote sensing, global internet services, and high-speed communications [3].

Along with the new space paradigm, the SAR imaging market has grown explosively owing to its irreplaceable imaging characteristics, which are independent of weather conditions and sunlight illumination, unlike electro-optic or infrared sensors [4]. In fact, the value of the SAR imaging market reached 4.5 billion USD in 2019, and it is anticipated to grow at a rate of 8.5% per year until 2026 [5]. In the new space era, this dramatic market

growth has triggered collaboration with developers of small SAR satellite constellations because the technological advances in electronics and SAR image processing as well as high revisit rates have made SAR payloads compatible with small satellite platforms, meaning that small SAR satellite constellations can substitute for large SAR satellite missions. Several examples of such collaboration that exploit small SAR satellite constellations [6–9] are given below. StriX- α is an X-band SAR satellite built by Synspecive as a model of their planned 25-satellite constellation. This is a 150 kg satellite with a ground resolution of 1–3 m [6]. Capella X-SAR is a 107 kg microsatellite. The satellites feature an X-band SAR with a resolution of 0.5 m, and which provides all-weather imagery using 3.5 m aperture-deployed mesh-based reflector antennas [7]. QPS-SAR is a series of small high-resolution X-band SAR satellites developed by the QPS Institute (iQPS). Such satellites are the precursors for a subsequent constellation mission with 36 satellites in on-orbit and, have a weight of 100 kg with a 3.6 m diameter antenna, which provides a 1 m resolution [8]. ICEYE-X2, which is a typical representative instrument of the ICEYE constellation, is a microSAR satellite that acquires SAR images using Stripmap, Spotlight, and ScanSAR modes with an active phased array X-band SAR antenna [9]. These small SAR satellites are currently being developed or are even operated in mission orbit. In addition, some small SAR satellites, such as ICEYE and Capella X-SAR, have recently provided practical SAR images from their mission orbits, whose resolutions are close to those of large-scale SAR satellites [10–12]. Such an achievement with small SAR satellite is due to the technical advancement of electronics and SAR image processing [13]. Therefore, in the upcoming new space era, it is anticipated that state-of-the-art and miniaturized electronics such as radar transmitters, receivers, and data handling modules will trigger the explosive use of small SAR satellites for spaceborne SAR imaging missions.

The Small SAR Technology Experimental Project (S-STEP) aims to develop an 80 kg-class ultralight weight X-band SAR satellite based on an active phased array antenna. The primary mission of the S-STEP is Earth observation, such as environmental investigation, surface mapping, and disaster monitoring. To acquire earth observation SAR imaging data, the S-STEP system provides a high resolution of 1 m Stripmap, 4-m ScanSAR, and 10 s continuous 1 m VideoSAR operational modes. As an SAR payload, an aperture-coupled cavity-backed micro-strip patch array antenna with high gain [14] is considered in the system design.

The S-STEP system has adopted various challenging strategies to aggressively pursue the new space philosophy, that is, faster, cheaper, better, and lighter. The major strategies are the bus-payload integrated flat plate-type platform, multi-functional structure of the transmit/receive (TR) module, dedicated vibration-free orbit deployer (VFOD), and unique thermal design concept. Among the abovementioned strategies, the key strategy is to develop a dedicated VFOD that provides a side-mounting launcher-ride interface together with multiple functions on the S-STEP system. The multiple functions of the VFOD are whole spacecraft vibration isolation and in-orbit satellite deployment. Here, the function of the whole spacecraft vibration isolation helps to reduce the total mass of the satellite by mitigating the launch design load transmitted to the satellite. This approach also saves development cost and contributes to the scheduling of the project by optimizing the conventional conservative space verification process [15], which occupies a large portion of the entire satellite development program. Furthermore, the optimization of the on-ground verification process, that is, streamlining and skipping the test phase or step at a subsystem level, could be considered. For instance, the verification can be carried out at a higher system level with an integrated scheme instead of a lower subsystem level because the function of the whole spacecraft vibration isolation of the VFOD can significantly mitigate the potential failures of the vibration-sensitive components. In addition, saving the test duration for notching [16] can be anticipated in the launch vibration test, which takes a large portion of the time to create an adequate notched profile. These potential advantages of the VFOD are attractive for the new space-based development trend to achieve the goal of cost-effective small satellite development. In the past, several studies with regard

to whole spacecraft vibration isolation have been reported [17,18]. In addition, the side-mounting launcher-ride interface of the VFOD is designed to be compatible with the off-the-shelf rideshare accommodation platform, for example, ESPA ring [19] or Dispenser ring of the SpaceX [20]. Thus, it enables to mount the number of four S-STEP on one 24" ESPA or 24" Dispenser ring. Therefore, using the VFOD, it is possible to launch multiple satellites simultaneously at a time for the S-STEP constellation mission, contributing to a drastic reduction in the launch cost. In this multiple-satellite accommodation configuration together with the ESPA or Dispenser ring, the VFODs are sequentially activated to function the in-orbit multiple satellite deployment. Such a side-mounting ride configuration of the satellite provides easier in-orbit coordination of the deployed multiple satellites by using only the spinning moment of the launcher and a restoring force of the compressive spring installed inside the VFOD; otherwise, the pitch-over maneuver of the launcher is not required [21]. Aside from these advantages, a stack configuration of multiple S-STEPs can be positively considered in the launch, such that more number of S-STEPs can be simultaneously put into mission orbit for future megaconstellation missions.

The design strategy of a bus-payload integrated flat plate-type structure without flexible deployable appendages helps to achieve a compact and high-dimensional stabilized structure with the SAR antenna in on-orbit extreme thermal environments. Such an integrated structure also provides good stability to the SAR antenna with respect to the reaction wheel jitter. In addition, easier integration and de-integration as well as the alignment of the SAR antenna can be expected during the satellite system-level assembly, integration, and test (AIT) phase.

The use of a multifunctional integrated structure is also a design strategy for the S-STEP system. This strategy utilizes the transmit/receive (TR) module for the active SAR function as a structural stiffener and heat dissipation radiator. Therefore, the satellite system can have an increased satellite stiffness without introducing an additional stiffness design in the bus platform. In addition, the heat dissipation radiator integrated with the TR module guarantees a long-term SAR image acquisition of 120 s regardless of left and right looking owing to a novel passive thermal design for the TR module.

In order to validate the effectiveness of the innovative thermo-mechanical design concept of the S-STEP, satellite system-level structural analysis considering launch and on-orbit environments was performed. The system-level launch environmental specifications utilized in the structural analysis, such as quasi-static load and random vibration, are derived from the envelope curve of the representative launcher environmental specifications, such as SpaceX [20], Vega-C [22], Soyuz [23], and Dnepr [24]. The SAR antenna pointing error analysis was also carried out considering the worst thermal gradient condition and reaction wheel jitter. Based on the results of the system-level random vibration analysis, an example of how the component-level environmental specifications are derived is also introduced for the conditions with and without the VFOD. The key strategy, so-called VFOD, is validated through launch vibration and deployment tests by using a development model (DM) of the VFOD together with the dummy S-STEP. The development test results were then introduced.

2. S-STEP System Overview

S-STEP aims to develop an 80 kg-class smaller, better, faster, and lighter SAR satellite based on a new space philosophy. The main mission objective of S-STEP is the on-orbit demonstration of a small SAR technology and the acquisition of high-resolution SAR images for environmental investigation, surface mapping, and disaster monitoring in near-real time.

Figure 1 shows the operational concept of the S-STEP mission. S-STEP provides a high-resolution stripmap image with a 1 m resolution to observe a wide range of areas of interest. It also provides ScanSAR mode with 4 m resolution and VideoSAR mode with 1 m resolution to track the varying conditions of an interesting target. The SAR antenna of the S-STEP satellite is an aperture-coupled cavity-backed microstrip patch array antenna that has

the advantage of high gain, as well as 192 TR module channels for implementing electrical beam-steering capability in the elevation direction. The acquired image is transmitted and stored in integrated avionics unit (IAU) through Wizard Link and transmitted to the ground station through an X-band downlink module at a maximum speed of 1 Gbps. In addition, the S-band inter-satellite link (ISL) is considered in the system design to correspond to the immediate communication link of satellites. Table 1 summarizes the specifications of the S-STEP system.

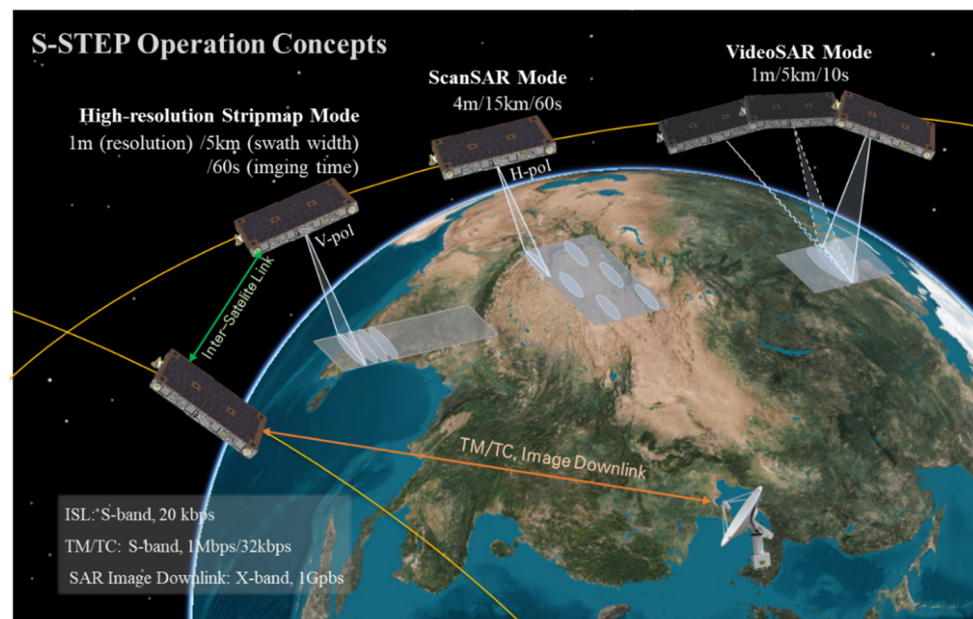


Figure 1. Mission operation concept of the S-STEP system.

Table 1. S-STEP system specification.

Specification		Value
Mission Lifetime		3 years
Mass		80.3 kg
Satellite Size		1970 mm × 1060 mm × 200 mm
Power	Generation	340 W (BoL)
	Save	648 Wh
Inter-Satellite Link		RF (S-band)
TM/TC/Image Downlink		S-band/X-band
Pointing Accuracy		0.085° (3σ)
Resolution (≈25°)		1 m (Stripmap), 4 m (ScanSAR) 1 m (VideoSAR)
Swath (elevation × azimuth)		5 km × 420 km (Stripmap), 15 km × 420 km (ScanSAR) 5 km × 5 km (VideoSAR)
Image Acquisition Time (one pass)		60 s (Stripmap), 10 s (VideoSAR)

Figure 2 shows the representative mass ratio of the S-STEP in the preliminary design review (PDR) phase. The structural mass ratio without considering the mass reduction by the isolation system is 17%, which is approximately 5% lower than that of a conventional satellite. If the design approach used in S-STEP, such as whole spacecraft vibration

isolation and the strain-based structural design methodology for electronics, are applied to commercial-off-the-shelf (COTS) products, which comprises 48% of the S-STEP system, a much greater mass reduction can be expected. The detailed new space-based mechanical design approach for S-STEP to achieve lightweight and low-cost satellites is described in Section 3.1.

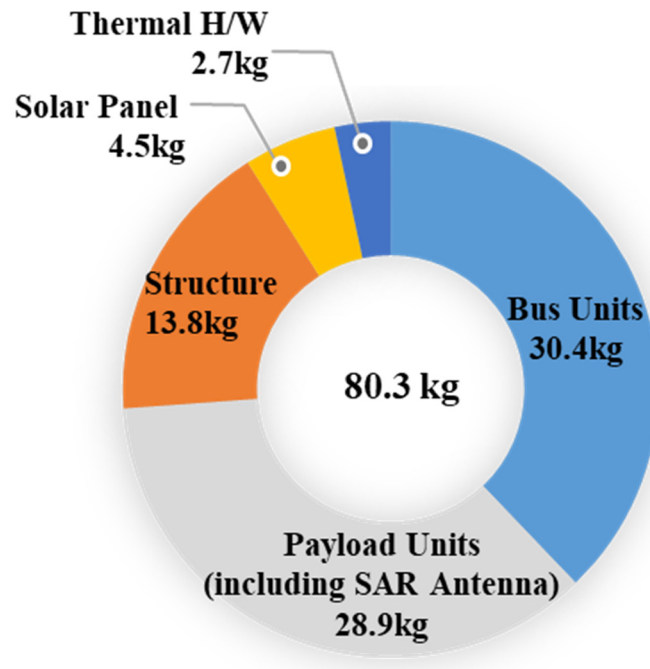


Figure 2. Mass ratio of the S-STEP system.

Figure 3a,b compares the performance index of new space SAR systems with traditional SAR systems with respect to satellite mass [25]. Here, Figure 3b shows the zoomed view of Figure 3a. The performance index calculated from the S-STEP system is also plotted in Figure 3a,b to evaluate the performance level and consistency with the new space trend of the S-STEP system currently being developed.

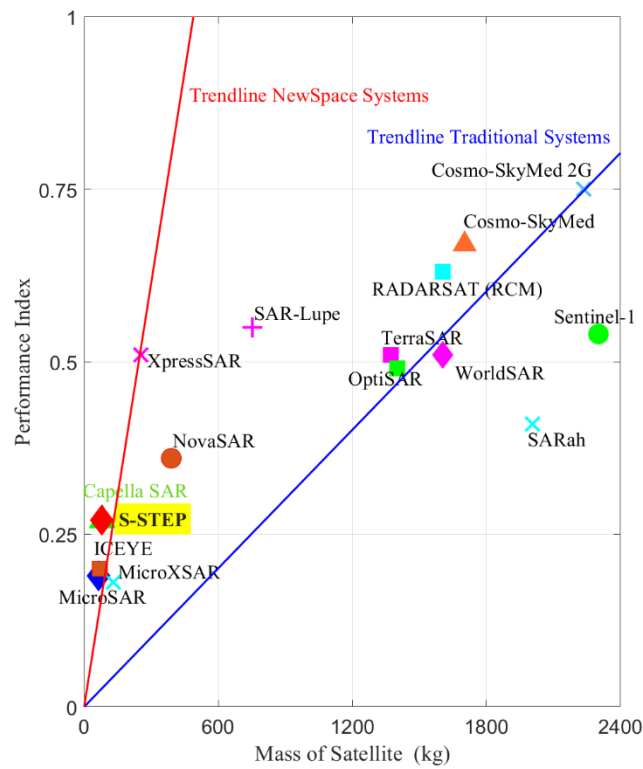
The SAR performance index, PI_{sat} , was calculated by:

$$PI_{\text{sat}} = \frac{RR + SW + AT + PP + P}{6} (\%), \quad (1)$$

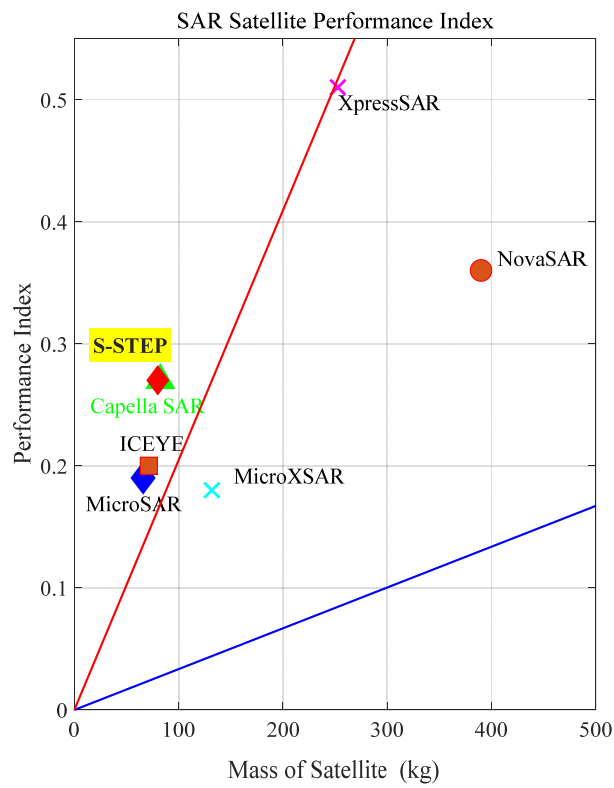
where RR is the range resolution, SW is the swath width, AT is the acquisition time, PP is the transmitted peak power, and P is the polarimetry. The parameters used in the calculation of Equation (1) are summarized in Table 2. The performance index of traditional SAR satellite systems is significantly higher than that of NewSpace systems. The index value obtained from the S-STEP system is also quite close to the New Space trend line for other representative small SAR satellites.

Table 2. S-STEP system performance parameter.

Frequency Band	Resolution	Swath Width	Acquisition Time	Peak Power	Mass
X-band	1 m	5 km	60 s	2560 W	80 kg



(a)



(b)

Figure 3. SAR performance index as a function of satellite mass, Adapted from [25] [(a): Overall View, (b): Zoomed View].

3. Innovative Mechanical Design for S-STEP

3.1. Development Philosophy

The S-STEP system has adopted various mechanical design strategies to aggressively trace the new space development philosophy. The major strategies are bus-payload integrated flat plate-type satellite platform without deployable appendages such as deployable solar panels and antennas, multifunctional TR module with the additional functions of a structural stiffener and heat dissipation to guarantee a long-term SAR imaging acquisition time, and a dedicated VFOD that provides dual functions of whole spacecraft vibration isolation and in-orbit satellite separation. The function of whole spacecraft vibration isolation serves to reduce the total mass of the satellite by mitigating the design load and the function of in-orbit satellite separation serves easier in-orbit coordination of multiple satellites. The unique thermal design concept of optimizing solar heat flux is also one of the design strategies to achieve a development philosophy of “lighter” by minimizing the system heater power budget. Aside from these major strategies, the S-STEP system has dealt with additional methodologies to further realize the “lighter” philosophy, such as the minimization of the holding and release mechanism, the optimization of structural parts by minimizing the structural margin, and the utilization of new critical-strain-based electronic design guides [26] to compensate for drawbacks of the conventional Steinberg’s theory [27] that results in the structural overdesign of electronics.

3.2. Thermo-Mechanical Design

Figure 4a,b show the rear ($-z$ - dir.) and front ($+z$ - dir.) views of the S-STEP system, respectively. The size of the S-STEP was $1970\text{ mm} \times 1060\text{ mm} \times 200\text{ mm}$, and its total mass was 80.3 kg . The mechanical configuration of the S-STEP is a flat plate-type structure, and the front and rear sides provide the interface for the active phased-array SAR antenna and the solar panel, respectively. From the perspective of the system-level AIT, this flat plate-type structure with the rear and front side interfaces provides easier integration and de-integration as well as the alignment process for the SAR antenna. Moreover, this makes the S-STEP simply stack up so that multiple satellites launch or environmental tests that are performed simultaneously under the stacked configuration can be positively taken into account if necessary. However, the rear side ($-z$ - dir.) of the structure also provides interfaces for the Frangibolt (2EA) launch locking device near the center and the VFOD at each corner. In this study, a design strategy that minimizes the use of a launch locking device can be achieved by the combination of the Frangibolt and the ball-and-socket-type interface between the satellite and the VFOD. More details regarding the ball-and-socket-type interface are discussed in below.

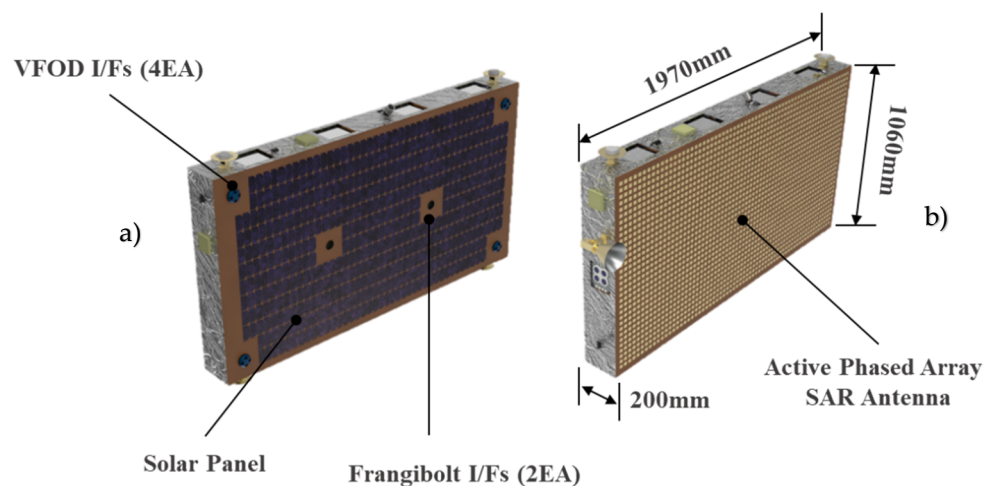


Figure 4. (a) Rear ($-z$ - dir.) and (b) front ($+z$ - dir.) view of the S-STEP.

Figure 5 shows an exploded view of the S-STEP system. The bus platform is mainly composed of aluminum skin honeycomb panels at the top and bottom sides, and these aluminum skin honeycomb panels (hereafter called composite) are assembled in parallel through the supporting brackets at each corner. In order to maximize the mass reduction of the satellite, a mechanical cutout is entirely implemented on the aluminum skin honeycomb panels, except for the electronics and payload attachment interface. At this point, it can be observed that the composite panel provides the interface for the electronics and payloads, meaning that the bus and payloads share the composite panel as an installation platform. Under an on-orbit extreme thermal environment, such a structure without deployable appendages can ensure high-dimensional stability on the SAR antenna. On the other hand, it can also be observed that four multifunctional TR modules are arranged in sequence between the top and bottom composite panels, and the radiator that is integrated at both sides of the TR module connects with the top and bottom composite panels. Such an installation of the multifunctional TR module contributes to an increase in the structural stiffness of the satellite. In addition, the radiator integrated at both sides of the TR module effectively dissipated the heat generated from the TR module activations. Therefore, the TR module can guarantee long-term SAR image acquisition for 120 s regardless of the left and right looking of the satellite. Based on this bus platform, which adopts innovative strategies, the symmetric placement of the on-board equipment, such as batteries, power control units, reaction wheels, is implemented to minimize the inertia moment of the satellite.

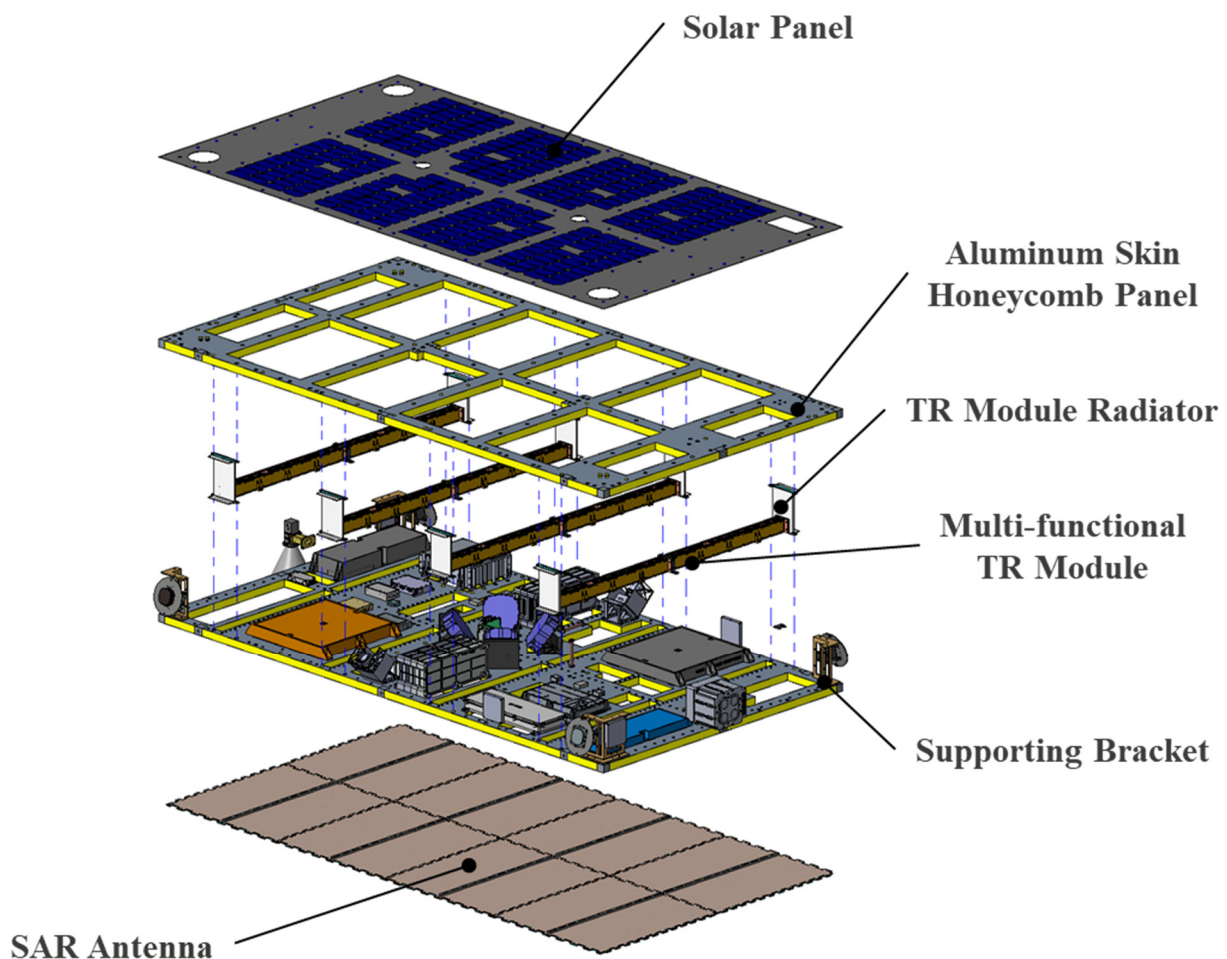


Figure 5. Exploded view of the S-STEP system.

Figure 6 shows the exploded cross-sectional view of the S-STEP system, VFOD, and launcher adaptor (for example, 24" dispenser ring of SpaceX [20]). The VFOD is mainly

composed of a CFRP honeycomb panel, whole vibration isolation system (4EA), and an in-orbit separation mechanism (4EA). In addition, the VFOD has a Frangibolt interface. During the launch phase, this Frangibolt rigidly connects the VFOD with the S-STEP, and the VFOD is gently suspended on the launcher adaptor through the whole spacecraft vibration isolation system. Such an isolation system simply adopts a passive method by utilizing a spring and damper system, putting the 1st eigenfrequency of the S-STEP system with the VFOD assembly at approximately 25 Hz to obtain the cut-off frequency effect [28] during launch. Therefore, vibration-free conditions in which the launch loads transmitted to the satellite are significantly mitigated can be implemented. On the other hand, when the Frangibolt is activated in the mission orbit, the notched part on the locking rod of the Frangibolt is broken such that the S-STEP system can be released from the VFOD by the restoration force of the compressive spring, which is installed inside the in-orbit separation mechanism placed at each corner of the VFOD (a detailed view of the in-orbit separation mechanism is shown in Figure 7). Here, it can be observed that the VFOD is still attached to the launcher adaptor even after the separation of the satellite, meaning that the mass of the VFOD is not considered in the mass budget of the S-STEP for on-orbit operation.

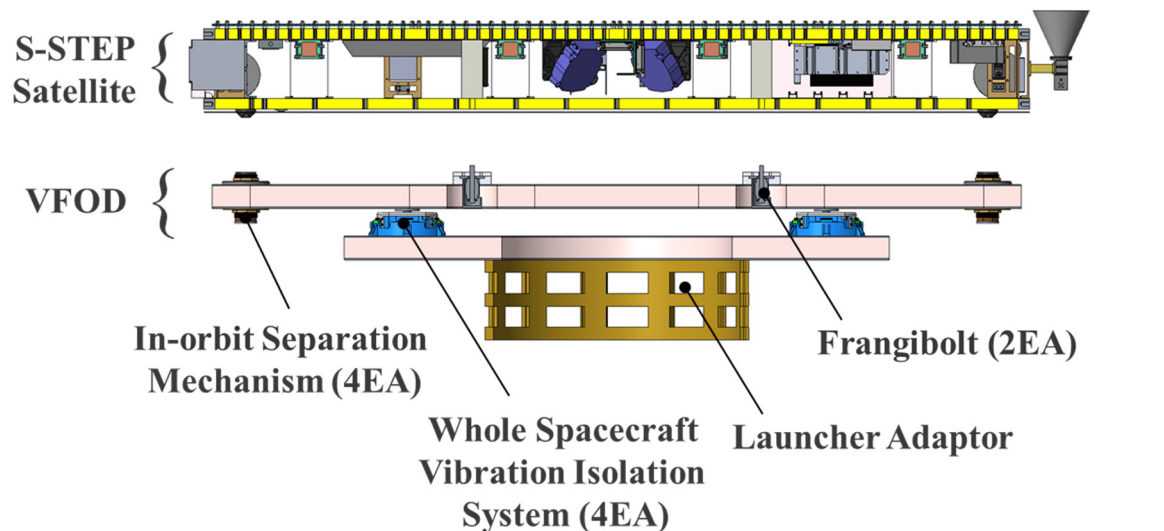


Figure 6. Exploded cross-sectional view of the S-STEP system, VFOD, and launcher adaptor.

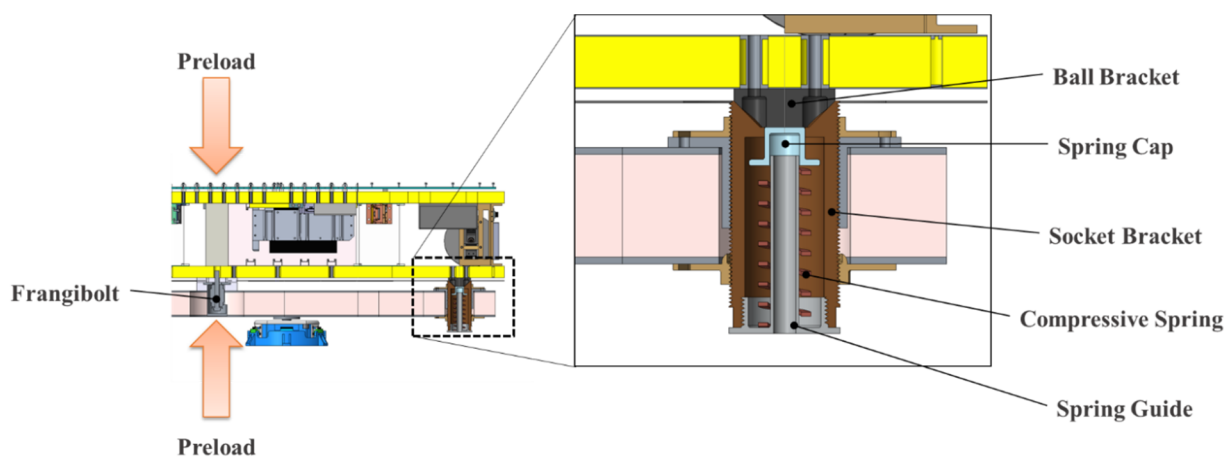


Figure 7. Zoomed cross-sectional view of the in-orbit separation mechanism of the VFOD.

Figure 7 shows the magnified cross-sectional view of the in-orbit separation mechanism placed at each corner of the VFOD, as shown in Figure 6. The mechanism is mainly

composed of ball-and-socket brackets, compressive springs, spring guides, and spring caps. Here, the ball bracket is attached to the satellite; otherwise, the rest are attached to the VFOD. For the launch configuration, these brackets are placed in close contact with each other using a preloaded Frangibolt. The preload is determined from a trade-off study that derived the effective preload ranges. The effective preload ranges can be obtained from the analysis of gapping and structural MoS for the ball and socket-brackets. Here, as the preload increases, the gapping between the ball-and-socket brackets minimizes otherwise the structural MoS for these brackets inversely decreases. Based on this analysis, the resultant preload ranges were determined to be 13,000–17,800 N so that non pyro-technic type Frangibolt[®]-FC6 was selected (TiNi[™] Aerospace [29]) for the launch locking device of the S-STEP system. Such a preload pushes down the compression spring inside the in-orbit separation mechanism via the spring cap, thereby pressing the spring during launch. In this condition, the shape of the ball-and-socket brackets helps to prevent the in-plane directional movement of the satellite. Moreover, each contact surface of the ball-and-socket brackets is secured by an elastic coating, namely, Everlube[®] 620C [30], which provides wear resistance, torque relaxation, interference fit improvement, and cold welding prevention in an on-orbit extreme cold environment. When the Frangibolt is activated in the on-orbit, the compressed spring inside the socket bracket travels along with the spring guide and injects the S-STEP system into the mission orbit by the restoration force of the compression spring. Here, the value of the spring constant is determined by considering a satellite separation velocity limit of <1 m/s.

Figure 8a shows the practical configuration of the side-mounting launcher-ride using a dispenser ring to launch multiple satellites named OG₂, which is a constellation communication satellite for machine-to-machine (M2M) and Internet of Things (IoT) solutions [31]. Figure 8b shows an example configuration of the S-STEP considering the side-mounting launcher-ride concept, as shown in Figure 8a. Under such a launch concept, four S-STEP systems can be implemented using the 24" dispenser ring of the SpaceX [20]. In addition, once the allowable accommodation volume of SpaceX is considered, 20 S-STEP systems can be simultaneously launched for the constellation mission.



(a)

Figure 8. Cont.

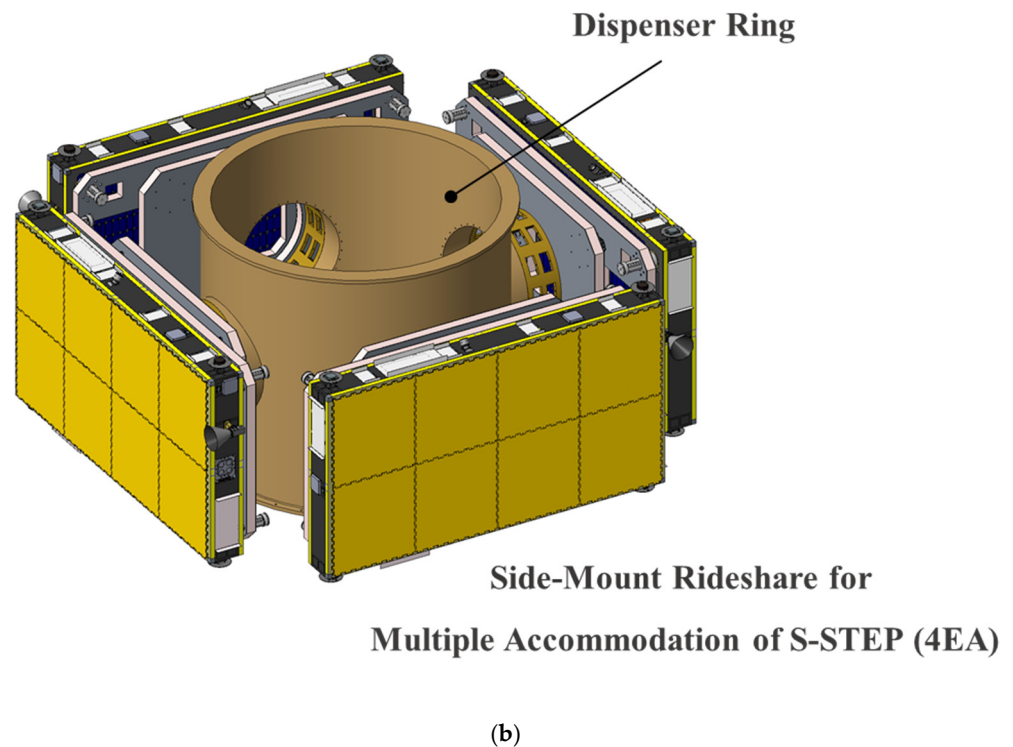


Figure 8. Side-mounting launcher-ride configuration using a dispenser ring to launch multiple satellites [(a): OG₂ satellite, Adapted from [31], (b): Example of the S-STEP].

Figure 9 shows the S-STEP system thermal control design concept. Thermal control is based on a passive method that uses thermal coating, multilayer insulation (MLI), and a heat dissipation radiator. In the thermal control design, the entire front surface of the SAR antenna as well as the side walls of the satellite platform, which has a relatively lower heat flux, are utilized for the heat dissipation area. In addition, a unique thermal design concept that optimizes the incoming solar heat flux through the solar panel and the radiating heat flux toward deep space through the SAR antenna is applied as one of the design strategies. This achieves a lightweight small satellite by minimizing the system heater power budget. Moreover, the radiator for the heat dissipation of the TR modules is positioned at the side wall of the satellite platform, where the effect of the heat flux is minimal.

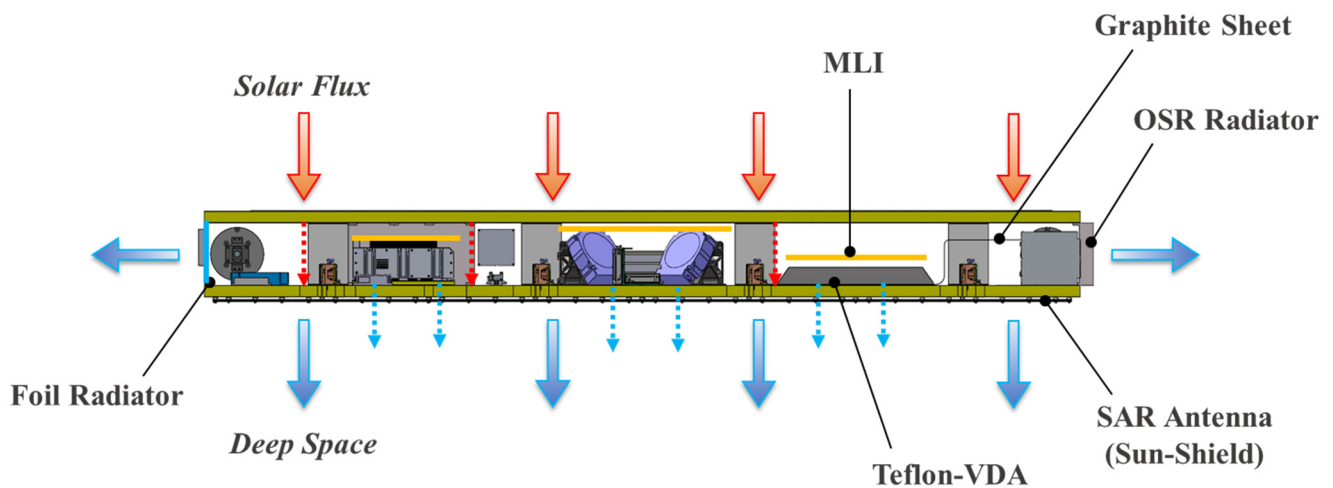


Figure 9. Thermal control design concept for the S-STEP system.

This design guarantees a long-term SAR image acquisition of 120 s, regardless of the left and right looking of the satellite. Furthermore, for the thermal design of high heat dissipation electronics such as batteries and power control unit, etc., a conductive thermal path between the electronics and the sidewall mounted radiator is implemented by using a relatively lighter thermal conduction material, namely, the so-called graphite sheet [32], instead of the conventional heat pipe [33].

4. Structural Analysis for S-STEP

4.1. Structural Analysis Overview

A satellite system-level structural analysis that considered launch and on-orbit environments was performed in order to validate the feasibility of the innovative thermo-mechanical design of the S-STEP system. The structural analysis cases are as follows: modal analysis, quasi-static analysis, thermo-elastic analysis, and random vibration analysis with and without the VFOD. The SAR antenna pointing error analysis with regard to the worst thermal gradient condition and reaction wheel jitter was also conducted. Based on the results of the system-level random vibration analysis, an example of how the component-level environmental specifications are derived is also introduced with respect to the condition with and without the VFOD.

The launch environmental specifications utilized in the system-level structural analysis, such as the quasi-static load, sine vibration, and random vibration are derived from the envelope curve of the representative launcher's environmental specifications, including SpaceX, Vega-C, Soyuz, and Dnepr. In the case of the design load for the S-STEP system, a 3σ rule [34] based on the acceptance level random vibration specification is used; therefore, the determined quasi-static design load is 24.7 g. On the other hand, the acoustic analysis and test are not considered in the S-STEP development program because the random vibration is more efficient way from the view point of small satellite development.

4.2. Structural Analysis Result

Figure 10 shows the finite-element model (FEM) of the S-STEP system, which is mainly composed of S-STEP and VFOD. In the FEM composition, PCOMP was utilized for the aluminum skin honeycomb panel and SAR antenna, PSHELL for the supporting bracket, solar panel, and radiator, and the lumped mass for the on-board equipment. Therefore, the total number of FEM elements was 118,401. The boundary conditions were divided into two configurations with regard to launch and on-orbit environments. Under the launch environment, the S-STEP system is rigidly fixed to the VFOD through the Frangibolts, and the VFOD is softly suspended on the launcher adaptor. Therefore, the Cbush element, which represents the stiffness and damping ratio of the Frangibolt and VFOD, was utilized to demonstrate each. Furthermore, the interface at ball-and-socket brackets was also implemented by the rigid-like Cbush element along with the translational directions (x -, y -, and z -axes) with the assumption that no gapping can occur owing to existence of the Frangibolt's preload; however, the rotational directions (rx -, ry -, and rz -axes) are set to free. A preload of 17,000 N, which was derived from the preliminary gapping analysis of the ball-and-socket brackets, was applied to the Cbush of the Frangibolt. The boundary condition for the constraint was applied to a launcher adaptor representative node with a six degree of freedom (DOF) fixation. Otherwise, under the on-orbit environment, the boundary condition is deleted in the FEM to demonstrate the on-orbit free-free configuration of the S-STEP. The FEM mass of the S-STEP and VFOD are, respectively, 85.3 kg and 23.22 kg, with the inclusion of a 10% contingency and miscellanea for the conservative analysis.

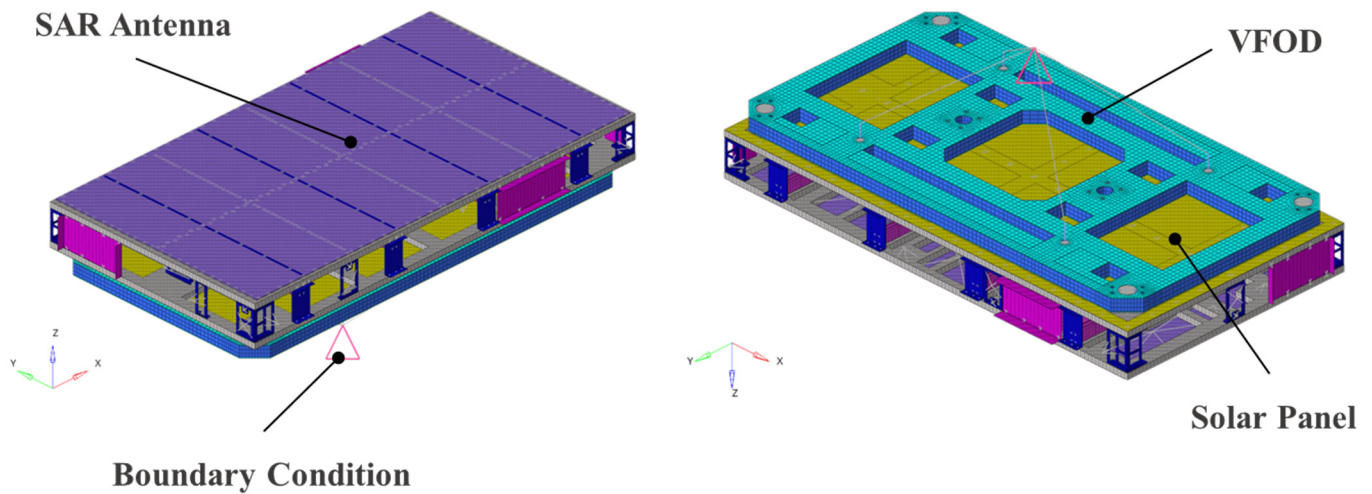


Figure 10. Finite-element model (FEM) of the S-STEP system.

Figure 11 shows the modal analysis results of the S-STEP under the launch configuration, where the S-STEP is rigidly clamped with the VFOD through the Frangibolt, and the VFOD is softly supported on the launch adaptor. Therefore, the 1st to 6th modes at approximately 25 Hz are rigid-body translational and rotational modes of the S-STEP assembly combined with the VFOD. The following 7th mode of 39 Hz is the local mode that results from the solar panel, and the 8th mode of 40.6 Hz is the first global bending mode of the S-STEP, which results from the global stiffness of the satellite structure rigidly clamped with the VFOD by a pair of Frangibolts (2EA). The result for the 8th mode indicates that only a pair of Frangibolts is sufficient to ensure a stiffness requirement of >35 Hz; thus, one of the design strategies that minimize the use of the launch lock mechanism to achieve “lighter” is also implemented as well. On the other hand, it can be observed that the 1st to 6th modes do not comply with the stiffness requirement. However, these rigid body motions result from the low-stiffened vibration isolation system under the VFOD, which is intentionally designed to have a low stiffness to mitigate the launch loads transmitted to the satellite.

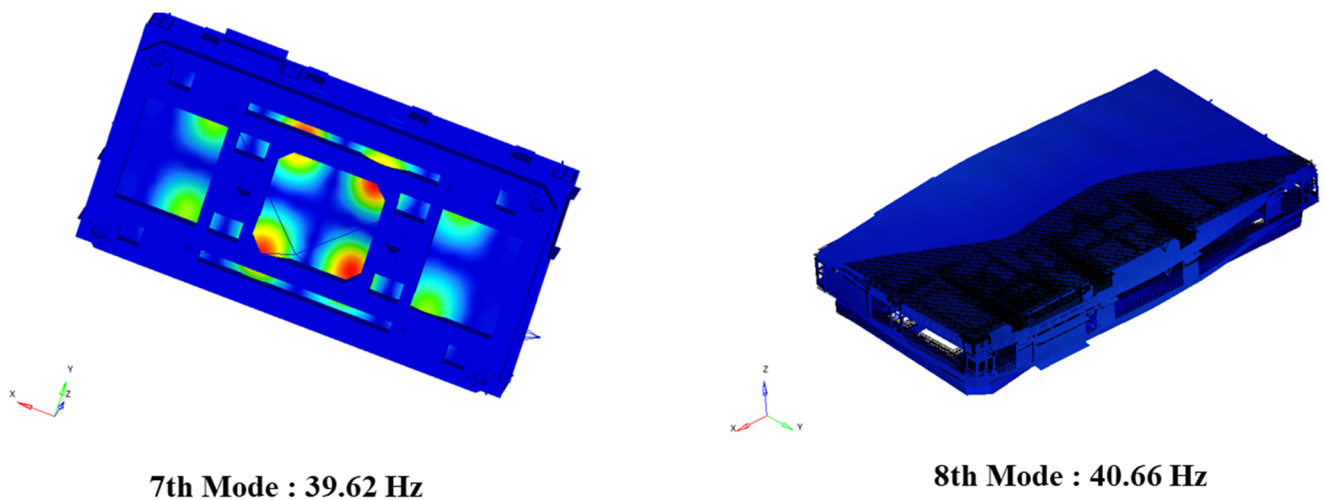
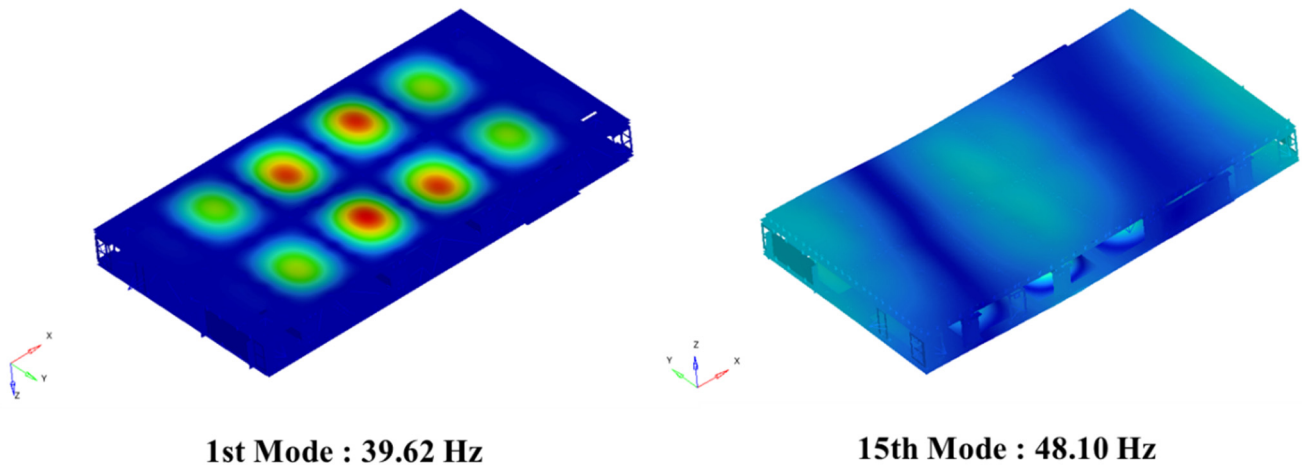


Figure 11. Modal analysis results obtained under the launch configuration.

Figure 12 shows the modal analysis results of the S-STEP under the on-orbit configuration, where the S-STEP is in a free-free condition without any constraints. Here, the 1st to 14th modes result from the solar panel. Aside from such a local mode, the 15th mode of

48 Hz is the first global bending mode of the S-STEP system, and this result complies with the stiffness requirement of >1 Hz under on-orbit conditions. This result also implies that the flat plate-type integrated structure without any deployable appendages can provide high stiffened configuration compared with the conventional satellite structure, which has deployable appendages, such as solar panels and antennas.



1st Mode : 39.62 Hz

15th Mode : 48.10 Hz

Figure 12. Modal analysis results obtained under the on-orbit configuration.

An important technical issue associated with the image quality of the SAR antenna is the thermal distortion of the antenna induced by temperature gradients in extreme space thermal environments [35]. This distortion causes an error in the surface contour of the SAR antenna, which degrades the radio frequency (RF) performance and antenna pointing accuracy. In order to evaluate the pointing error of the SAR antenna under an extreme on-orbit thermal environment, system-level distortion analysis was performed using the worst thermal gradient condition, which can result from the worst-condition on-orbit thermal analysis of the S-STEP system. The mechanical pointing error requirements of the SAR antenna, such as the antenna surface deformation RMS and antenna best-fit plane angle (ABFP), are derived from $\lambda/20$ and the S-STEP system requirement, respectively, and each are $<1.55 \text{ mm}_{\text{rms}}$ and $<0.02^\circ$, respectively. Here, λ is the wavelength of the SAR antenna. Figure 13 shows the representative worst thermal gradient contours of the satellite platform, SAR antenna, and solar panel during the SAR imaging operation mode in the worst cold case. As shown in the figure, the maximum ΔT of the satellite platform is 69.86°C between the upper and lower aluminum honeycomb panels. The maximum ΔT values of the SAR antenna and solar panel are 37.12°C and 7.55°C , respectively. These thermal gradient contours are then entirely mapped into the FEM using the linear interpolation method to compensate for the meshing difference between the thermal mathematical model (TMM) and FEM. Subsequently, thermal distortion of the SAR antenna under the worst thermal gradient condition can be achieved, as shown in Figure 14. In this result, the RMS value of the SAR antenna along the z-direction, where its direction is the worst one in terms of the pointing accuracy, is $0.7 \text{ mm}_{\text{rms}}$ and this result is much lower than that of the SAR antenna pointing budget requirement of $1.55 \text{ mm}_{\text{rms}}$ by a factor of 2.2. In addition, Figure 15 shows the representative SAR antenna ABFP along with the antenna longitudinal axis (x-axis) resulting from the worst thermal gradient. In this result, the ABFP angle can result from the first-degree polynomial with respect to the deformed shape of the SAR antenna, and the slope of the ABFP denotes the ABFP angle. Here, the resultant ABFP angle is 0.005° , and its value is significantly lower than that of the requirement of 0.02° by a factor of 4.

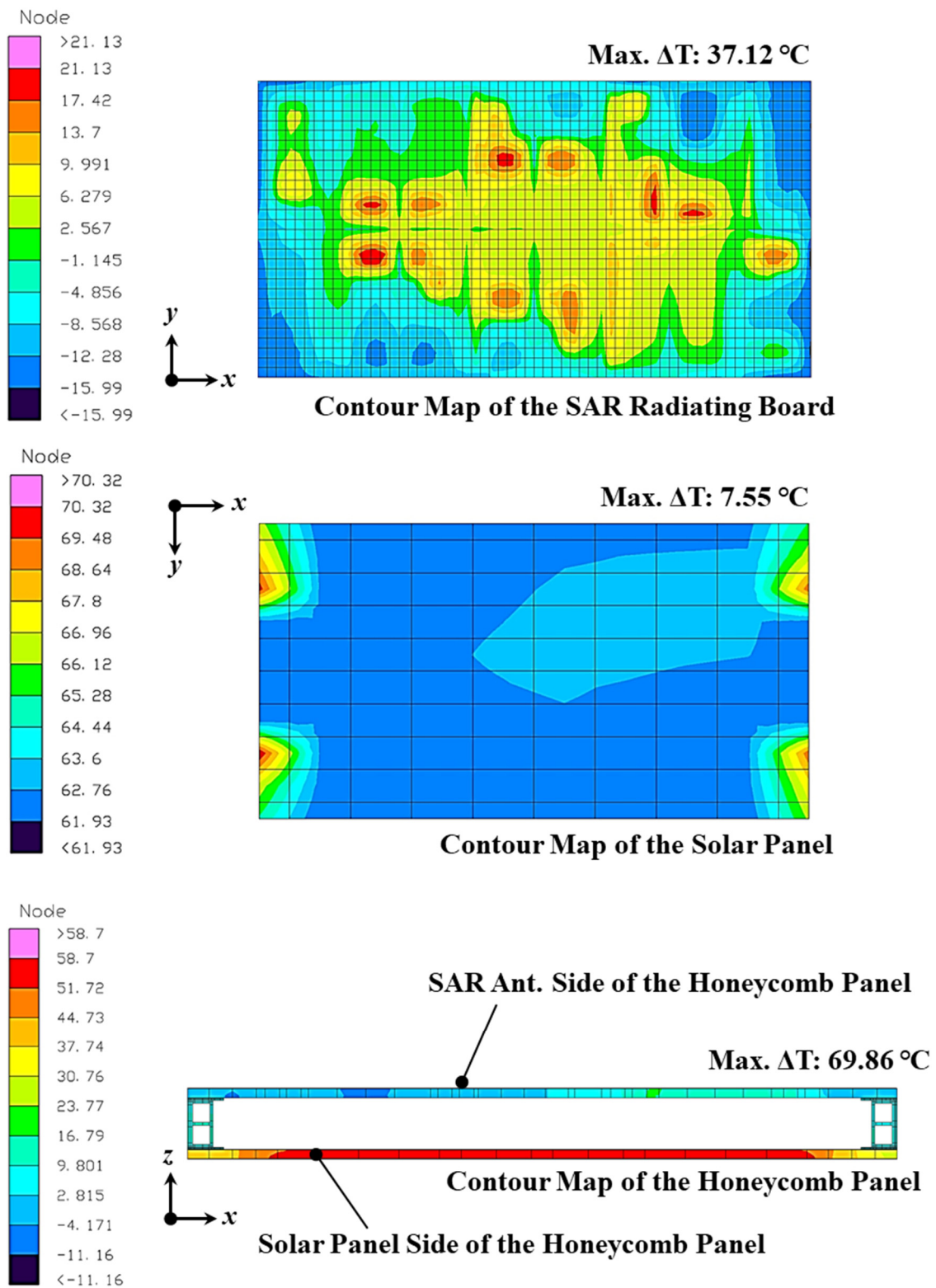


Figure 13. Worst thermal gradient contours of the satellite platform, SAR antenna, and solar panel during the SAR imaging operation mode in the worst cold case.

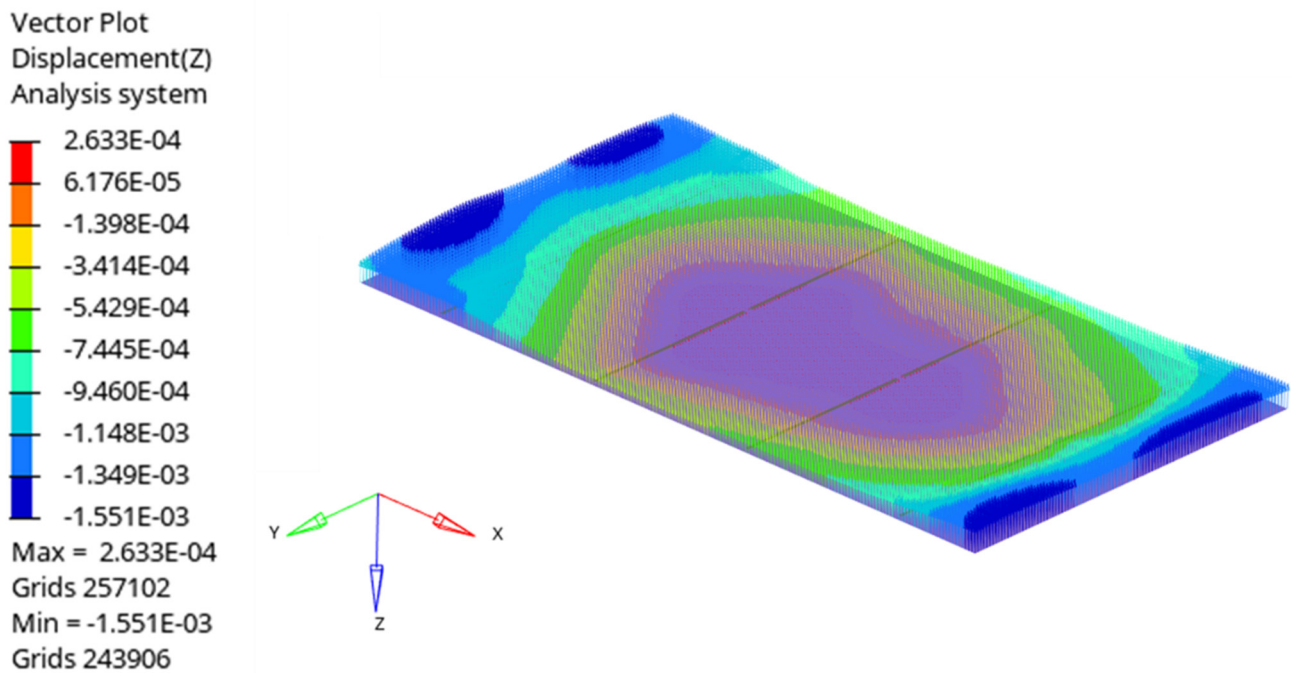


Figure 14. Thermal distortion of the SAR antenna under the worst thermal gradient condition.

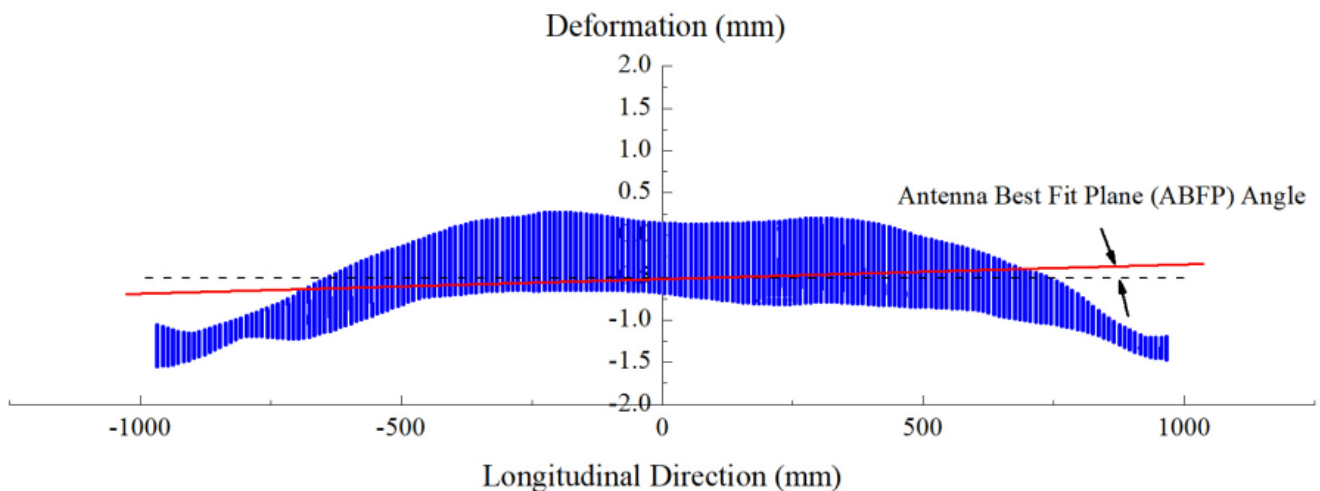


Figure 15. SAR antenna ABFP angle along the antenna longitudinal axis (x -axis) resulting from the worst thermal gradient condition.

The reaction wheel jitter is also one of the main contributors that degrade the pointing accuracy of the SAR antenna. Thus, SAR antenna pointing error analysis with respect to reaction wheel jitter is performed as well by using candidate reaction wheel jitter data [36]. Figure 16 shows the y -directional rotational angles of the SAR antenna with respect to the frequency spectrum. Here, the rotational angle of the SAR antenna used in the reaction wheel jitter pointing error analysis indicates the \pm end tips of the antenna. As shown in the figure, the rotational angle of the SAR antenna at the \pm end tips indicates that the result does not exceed the jitter requirement of 0.02° over the entire frequency spectrum. In this result, the peak rotational angle at 1 Hz is 0.003° , which is 6.7 times lower than that of the requirement. The high stability of the SAR antenna is due to the design strategy of the high-dimensional stability structure without any deployable appendages.

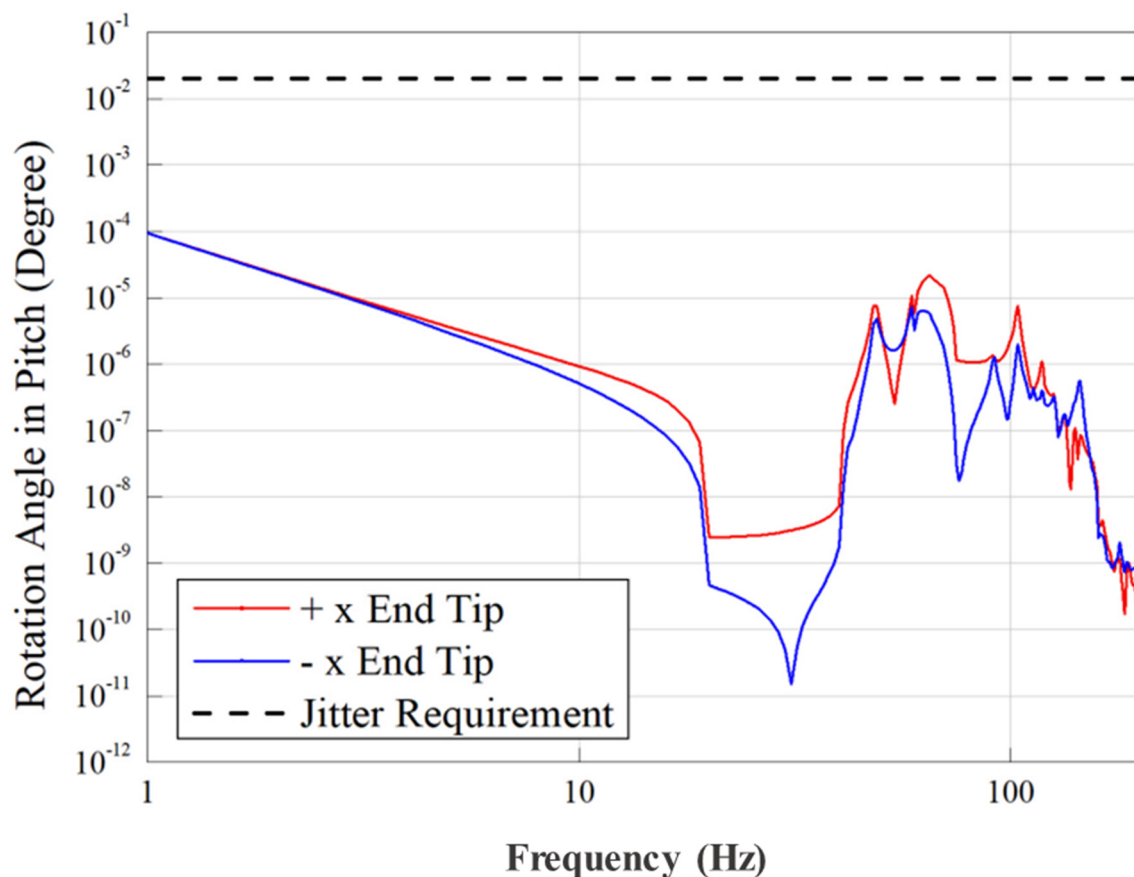
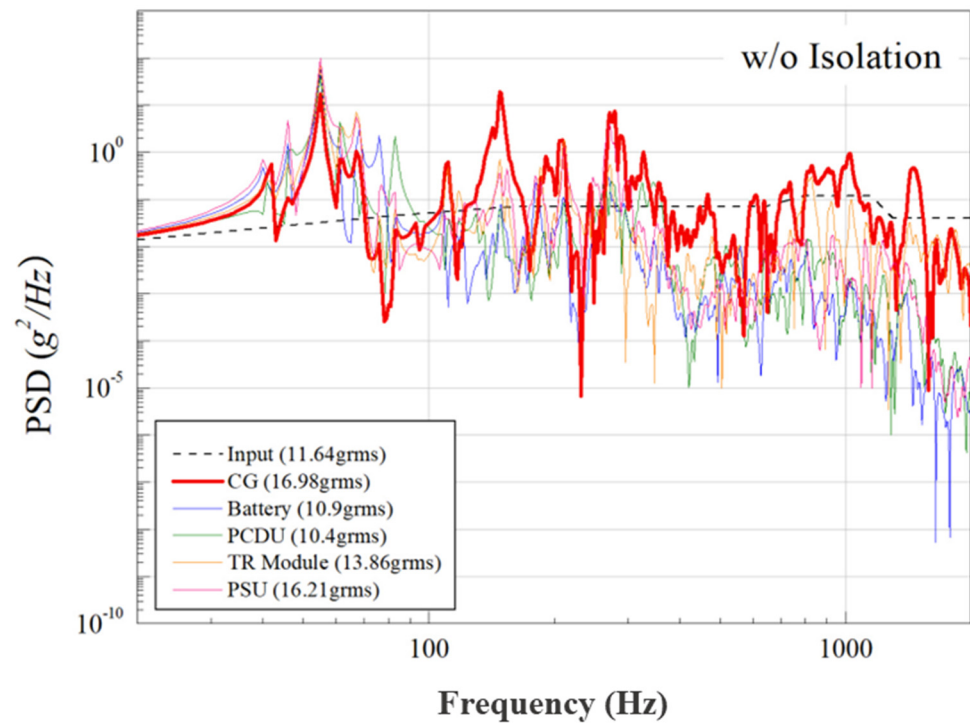


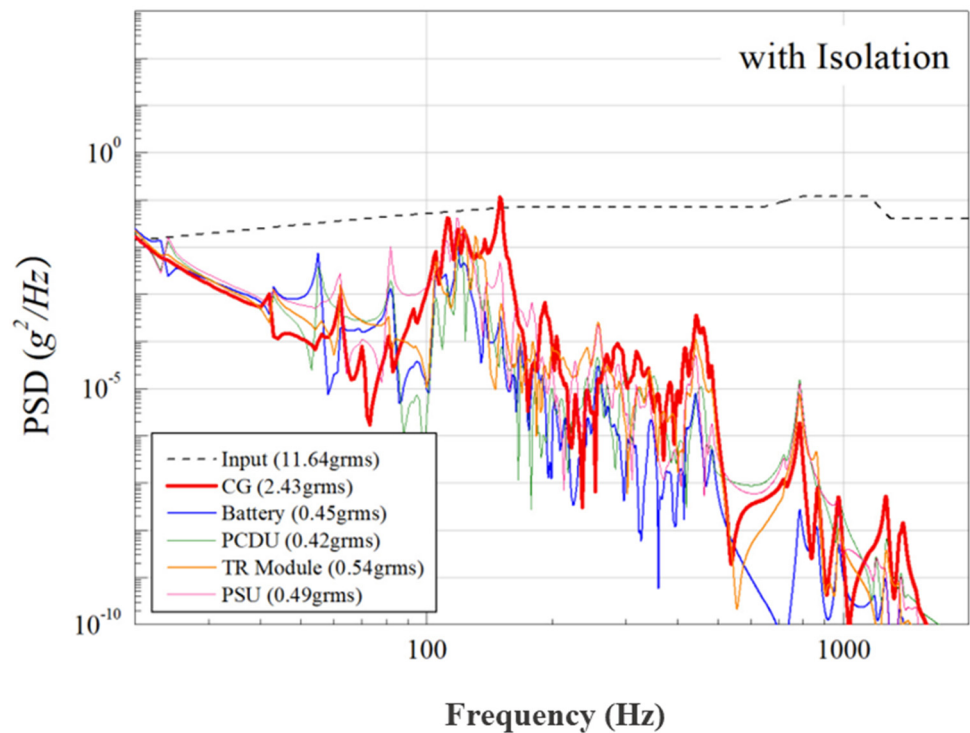
Figure 16. y -directional rotational angles of the SAR antenna \pm end tips with regard to the reaction wheel jitter.

In terms of the system pointing budget, these mechanical error sources, that is, the thermal gradient and reaction wheel jitter, are the major contributor that dominantly degrades the pointing accuracy of the satellite [37]. Therefore, the worst conditions, that is, the worst thermal gradient together with the reaction wheel jitter, may occur together in the S-STEP system, are qualitatively investigated. From the results obtained, the summation of the pointing error of the SAR antenna from the worst condition above is 0.008° , and this value still has a sufficient margin from the requirement.

Figure 17a,b show the random vibration analysis responses for all payloads, including the center of gravity (CoG) of the satellite with respect to the case both with and without the whole spacecraft vibration isolation in the VFOD. In this figure, the qualification level random vibration input is resulted from +3 dB based on the envelope curve of the representative launcher's specifications, and the resultant qualification random vibration level is 11.64 grms. On the other hand, all of the responses without vibration isolation of the VFOD are largely amplified above the qualification level random vibration specification. Otherwise, the responses with the vibration isolation of the VFOD show a drastic decrease based on the cut-off frequency; thus, high-frequency responses are all significantly isolated. For example, the CoG responses with respect to the case both with and without the vibration isolation of the VFOD are 2.43 grms and 16.98 grms, respectively, and the reduction ratio of the analysis result is approximately 7 according to the frequency cut-off effect of the VFOD. Based on these grms results, the estimated 3σ values are 50.9 g and 7.3 g, respectively. The value of 50.9 g significantly exceeds the quasi-static design load of 24.7 g by a factor of 2. Thus, an additional notching task should be considered during the test to ensure the structural safety of the satellite. However, under the condition with the vibration isolation of the VFOD, the resultant 3σ value of the satellite CoG is only 7.3 g, and its value is much lower than that of the pre-determined design load by a factor of approximately 3.4.



(a)

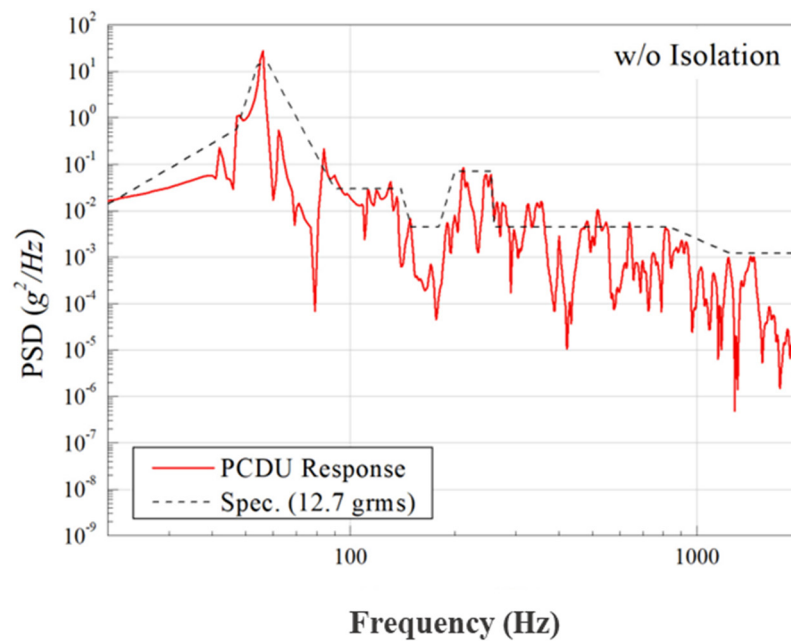


(b)

Figure 17. Random vibration analysis responses of the S-STEP system with respect to both with and without the whole spacecraft vibration isolation of the VFOD [(a): w/o isolation, (b): with isolation].

An example of how the component-level environmental specifications are derived is introduced herein with regard to the condition both with and without the vibration isolation of the VFOD, based on the results of the system-level random vibration analysis shown in Figure 17. The specification generation rule follows NASA GSFC Code 542 [38].

Figure 18a,b show the generated random vibration specifications of the power control divide unit (PCDU), which is one of the in-house design units, with respect to the conditions both with and without the vibration isolation of the VFOD. As shown in the figure, the specification curve with the isolation is much less than that without isolation, especially in the high-frequency range. The specification levels with and without the isolation are 1.1 grms and 12.7 grms, respectively. Based on these values, the quasi-static design loads of the PCDU are 3.3 g and 38.1 g, respectively. This result means that the specification reduction ratio is 11.5 times. As a result, the following advantages can be expected by utilizing the whole spacecraft vibration isolation with the VFOD. For example, the mitigation of potential failures in vibration-sensitive appendages, the optimization of the on-ground verification process, notching process omission, the minimization of a development model, and the decrease in the COTS procurement cost owing to reductions in the specifications. In addition, the total mass reduction of the satellite system resulting from the decrease in the design load for the satellite as well as the on-board appendages can be positively expected to be up to 29% for the satellite platform structure and 12% for the in-house development electronics. For example, the total mass of the satellite platform structure and in-house development electronics are 13.8 kg and 27.93 kg, respectively, and this mass can decrease up to 9.8 kg and 24.58 kg. Thus, a total of 7.35 kg can be further unweighted from the S-STEP system mass budget. These outstanding advantages of the whole spacecraft vibration isolation of the VFOD are very attractive for the new space-based development trend to achieve the goal of cost-effective, lightweight small satellite development.



(a)

Figure 18. Cont.

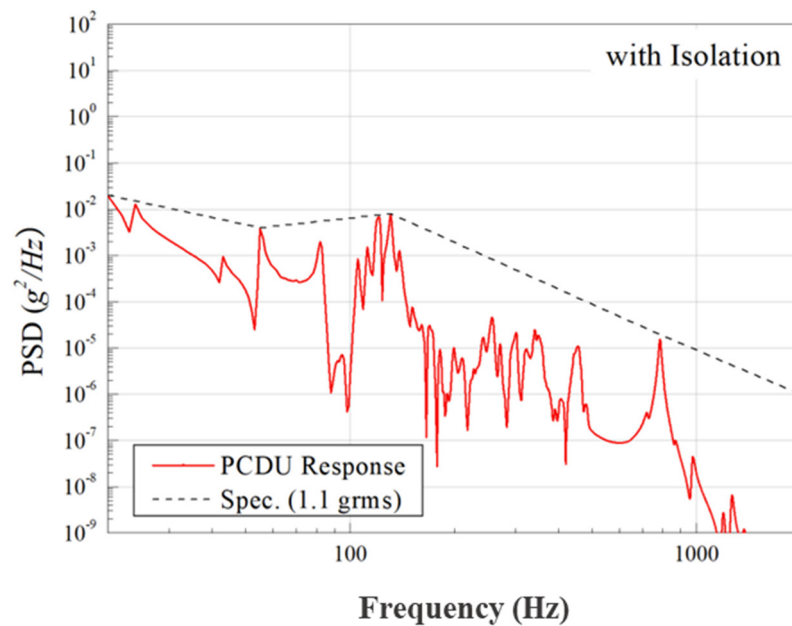


Figure 18. Generated random vibration specification of the power control divide unit (PCDU) with respect to both with and w/o the whole spacecraft vibration isolation of the VFOD [(a): w/o isolation, (b): with isolation].

5. Development Test for Key Strategy

5.1. Development Test Overview

The key strategy, so-called VFOD, is validated through launch vibration and satellite deployment tests using a development model (DM) of the VFOD, together with the dummy model of the S-STEP. The dummy model of the S-STEP is designed considering the mass, CoG, and the 1st eigenfrequency with dummy design requirements. In this study, the Frangibolt simulating device was designed to simulate the preload of the Frangibolt, that is, 17,000 N, and such a simulation device was only used during the launch vibration test to rigidly hold the dummy satellite with the VFOD. During the vibration test, the qualification level launch vibration specifications were used. A rigid-type mount was also applied to replace the whole spacecraft vibration isolation system under the VFOD in order to compare the vibration isolation performance of the VFOD as well.

5.2. Development Test Result

Figure 19 shows the launch vibration test setup of the VFOD with the dummy model of the S-STEP for the x -axis. In the test, the conditions with and without vibration isolation of the VFOD were tested for comparison by simply replacing the soft and rigid mounts under the VFOD. Figure 20 shows the representative random vibration test result of the dummy satellite's CoG under the 0 dB qualification level random vibration specification. As shown in the figure, the response without the isolation is approximately 14 grms and its 3σ value is 42 g, which significantly exceeds the design load of the S-STEP by a factor of 1.7. Thus, an additional notching task must be considered during the test to guarantee the structural safety of the satellite together with the on-board appendages, meaning that additional test schedules are inevitably wasted. Otherwise, the response with the isolation condition is just 3.2 grms even if the qualification level random vibration level is 11.64 grms. Therefore, its design load is only 9.6 g, and no additional notching task is necessary. In addition, its output response is significantly lower than that for the condition without vibration isolation by a factor of 4.4 owing to the frequency cut-off effect of the low-stiffened

suspend configuration of the VFOD such that any potential failures on the S-STEP system as long as the main payload can be avoided during severe launch vibrations.

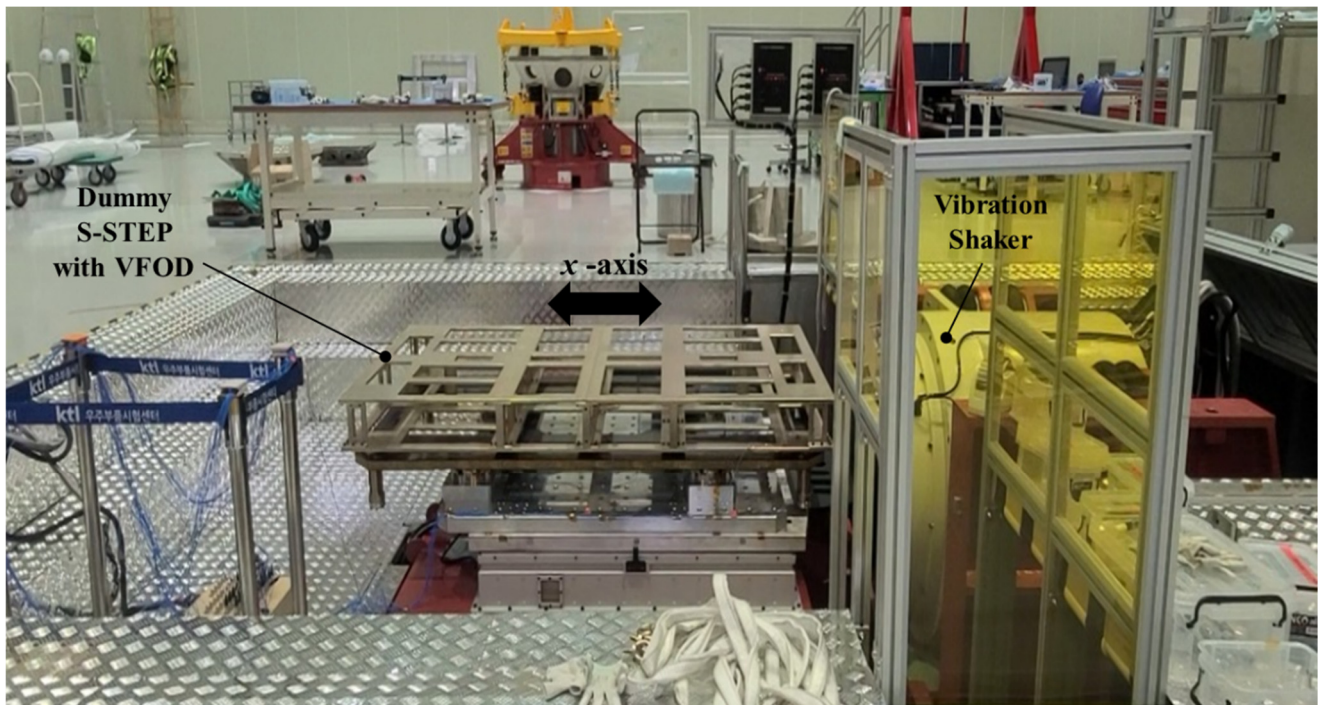


Figure 19. Launch vibration test setup of VFOD with dummy S-STEP for x -axis excitation.

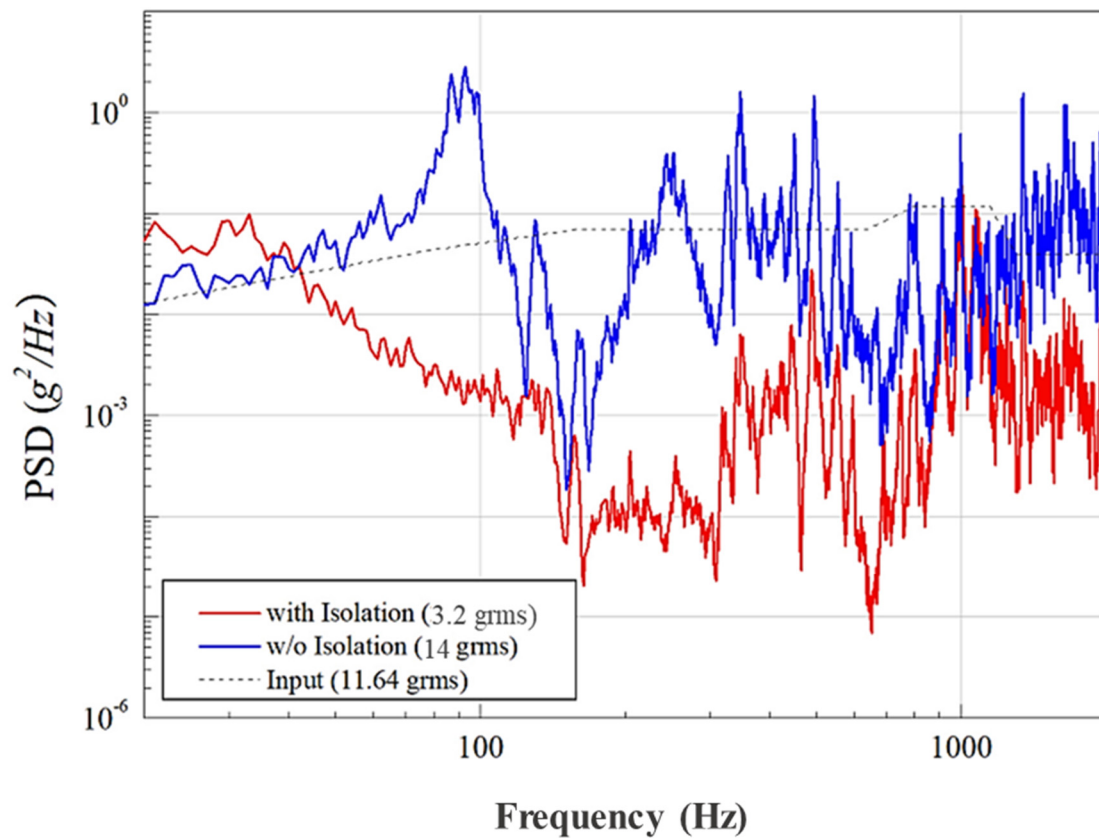


Figure 20. Random vibration test result of the dummy S-STEP's CoG under qualification level random vibration specification.

Figure 21 shows the satellite separation test results with respect to each time interval. Such a test was performed before and after the vibration tests to validate the repeatability of the satellite separation function of the VFOD without any functional failures during the launch vibration test, such as spring damage, stuck ball-and-socket brackets due to launch load-induced misalignment or welding problems on the coating material. In the separation test, a pair of strings hoists the satellite as much as the satellite mass by calibrating the load cell to compensate for the effect of gravity effect during the release sequence. In addition, to simulate the worst separation condition, only a single launch lock device was implemented between the satellite and VFOD. As shown in the figure, the satellite is successfully separated even after the vibration test, and its separation velocities before and after the launch vibration test are approximately 0.32 and 0.3 m/s, respectively, where both values are nearly identical and comply with the satellite separation velocity requirement of <1 m/s.

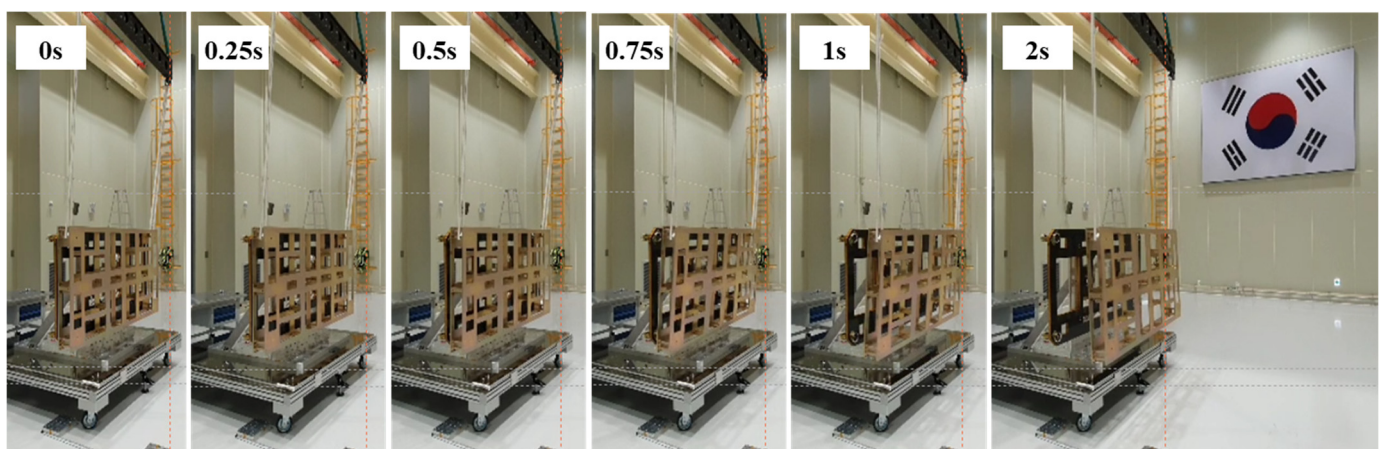


Figure 21. Satellite separation test result with respect to each time interval.

From the above test results, the feasibility of the key strategy, VFOD, has been verified, and its results are expected to significantly contribute to the upcoming space paradigm for the development of faster, cheaper, better, and lighter small SAR satellites.

6. Conclusions

In this study, an innovative thermo-mechanical design approach was proposed and investigated to develop a new space-based 80 kg-class X-band SAR satellite. The major design approaches, that is, the bus-payload integrated flat plate-type structure, multifunctional TR module with additional functions of a structural stiffener and heat dissipation, and the unique thermal design concept of using solar heat flux, have been verified by performing system-level structural analysis. In addition, the key strategy of VFOD, which provides the dual functions of whole spacecraft vibration isolation and multi satellite in-orbit deployment, has been verified using development tests, that is, launch vibration tests and satellite separation tests. The attractive validation results of the innovative thermo-mechanical design can promisingly put the S-STEP system into an upcoming new space era.

Author Contributions: Writing—original draft preparation, S.-C.K.; writing—review and editing, S.-C.K. and H.-U.O.; data curation, J.-H.S. and J.-H.P.; supervision, K.-R.K.; project administration, H.-U.O.; funding acquisition, S.-C.S. All authors have read and agreed to the published version of the manuscript.

Funding: This research was funded by the Agency for Defense Development (ADD).

Data Availability Statement: Not applicable.

Conflicts of Interest: The authors declare no conflict of interest.

References

1. Howard, E.M. *Faster, Better, Cheaper: Low-Cost Innovation in the U.S. Space Program*; The Johns Hopkins University Press: Baltimore, MD, USA, 2003.
2. Sweeting, M.N. Modern Small Satellites-Changing the Economics of Space. *Proc. IEEE* **2018**, *106*, 343–361. [CrossRef]
3. Ince, F. Nano and micro satellites as the pillar of the “new space” paradigm. *J. Aeronaut. Space Technol.* **2020**, *13*, 207–221.
4. Kuze, A.; Suto, H.; Nakajima, M.; Hamazaki, T. Thermal and near infrared sensor for carbon observation Fourier-transform spectrometer on the Greenhouse Gases Observing Satellite for greenhouse gases monitoring. *Appl. Opt.* **2009**, *48*, 6716–6733. [CrossRef] [PubMed]
5. Available online: <https://www.gminsights.com> (accessed on 7 March 2021).
6. Available online: <https://www.synspective.com> (accessed on 7 March 2021).
7. Farquharson, G.; Woods, W.; Stringham, C.; Sankarambadi, N.; Riggi, L. The Capella Synthetic Aperture Radar Constellation. In Proceedings of the IGARSS 2018–2018 IEEE International Geoscience and Remote Sensing Symposium, Valencia, Spain, 22–27 July 2018; pp. 1873–1876.
8. Available online: <https://www.i-qps.net> (accessed on 7 March 2021).
9. Ignatenko, V.; Laurila, P.; Radius, A.; Lamentowski, L.; Antropov, O.; Muff, D. ICEYE Microsatellite SAR Constellation Status Update: Evaluation of First Commercial Imaging Modes. In Proceedings of the IGARSS 2020–2020 IEEE International Geoscience and Remote Sensing Symposium, Waikoloa, HI, USA, 26 September–2 October 2020; pp. 3581–3584.
10. Covello, F.; Battazza, F.; Coletta, A.; Lopinto, E.; Fiorentino, C.; Pietranera, L.; Valentini, G.; Zoffolia, S. COSMO-SkyMed an existing opportunity for observing the Earth. *J. Geodyn.* **2010**, *49*, 171–180. [CrossRef]
11. Morena, L.C.; James, K.V.; Beck, J. An introduction to the RADARSAT-2 mission. *Can. J. Remote. Sens.* **2004**, *30*, 221–234. [CrossRef]
12. Torres, R.; Snoeij, P.; Geudtner, D.; Bibby, D.; Davidson, M.; Attema, E.; Potin, P.; Rommen, B.; Floury, N.; Brown, M.; et al. GMES Sentinel-1 mission. *Remote Sens. Environ.* **2012**, *120*, 9–24. [CrossRef]
13. Zhou, F.; Yang, J.; Jia, L.; Yang, X.; Xing, M. Ultra-High Resolution Imaging Method for Distributed Small Satellite Spotlight MIMO-SAR Based on Sub-Aperture Image Fusion. *Sensors* **2021**, *21*, 1609. [CrossRef] [PubMed]
14. Sun, D.; Dou, W.; You, L.; Yan, X.; Shen, R. A Broadband Proximity-Coupled Stacked Microstrip Antenna With Cavity-Backed Configuration. *IEEE Antennas Wirel. Propag. Lett.* **2011**, *10*, 1055–1058. [CrossRef]
15. Wijker, J.J. *Spacecraft Structures*; Springer Science and Business Media: New York, NY, USA, 2008.
16. European Space Community. *Space Engineering: Spacecraft Mechanical Loads Analysis Handbook*; ECSS Secretariat ESA-ESTEC: Noordwijk, The Netherlands, 2013; ECSS-HB-32-26A.
17. Jun, Z.; Hongxing, H.; Zhiyi, Z. An evaluation of the whole-spacecraft passive vibration isolation system. *Proc. Inst. Mech. Eng. Part G J. Aerosp. Eng.* **2007**, *221*, 67–72. [CrossRef]
18. Johnson, C.D.; Wilke, P.S.; Pendleton, S.C. SoftRide vibration and shock isolation systems that protect spacecraft from launch dynamic environments. In Proceedings of the 38th Aerospace Mechanisms Symposium, Williamsburg, Virginia, 17–19 May 2006.
19. Available online: <https://www.csaengineering.com> (accessed on 20 March 2021).
20. Available online: <https://www.spacex.com> (accessed on 20 March 2021).
21. Ping, L.; David, N.; Shelly, S.; Kenneth, H.; John, S. Pitch-over maneuver and guidance for rocket-back boosters. AIAA Guidance. In Proceedings of the Navigation and Control Conference, Portland, OR, USA, 8–11 August 2011.
22. Available online: <https://www.arianespace.com> (accessed on 20 March 2021).
23. Available online: <https://www.kosmotras.ru> (accessed on 20 March 2021).
24. Available online: <https://www.jaxa.jp> (accessed on 20 March 2021).
25. Filippazzo, G.; Dinand, S. The potential impact of small satellite radar constellations on traditional space systems. In Proceedings of the 5th Federated and Fractionated Satellite Systems Workshop, Toulouse, France, 2–3 November 2017.
26. Park, T.-Y.; Oh, H.-U. New PCB strain-based structural design methodology for reliable and rapid evaluation of spaceborne electronics under random vibration. *Int. J. Fatigue* **2021**, *146*, 106147. [CrossRef]
27. Steinberg, D.S. *Vibration Analysis for Electronic Equipment*, 3rd ed.; Wiley-interscience: Hoboken, NJ, USA, 2000.
28. Kwon, S.-C.; Jo, M.-S.; Ko, D.-H.; Oh, H.-U. Viscoelastic multilayered blade-type passive vibration isolation system for a spaceborne cryogenic cooler. *Cryogenics* **2020**, *105*, 102982. [CrossRef]
29. Available online: <https://www.ebad.com> (accessed on 25 March 2021).
30. Available online: <https://www.everlubeproducts.com> (accessed on 25 March 2021).
31. Available online: <https://www.orbcomm.com> (accessed on 25 March 2021).
32. Park, D.; Miyata, K.; Nagano, H. Thermal design and validation of radiation detector for the ChubuSat-2 micro-satellite with high-thermal-conductive graphite sheets. *Acta Astronaut.* **2017**, *136*, 387–394. [CrossRef]
33. Shukla, K.N. Heat Pipe for Aerospace Applications—An Overview. *J. Electron. Cool. Therm. Control.* **2015**, *5*, 1–14. [CrossRef]
34. Miles, J.W. On structural fatigue under random loading. *J. Aeronaut. Sci.* **1954**, *21*, 753–762. [CrossRef]
35. Park, T.-Y.; Kim, S.-Y.; Yi, D.-W.; Jung, H.-Y.; Lee, J.-E.; Yun, J.-H.; Oh, H.-U. Thermal Design and Analysis of Unfurlable CFRP Skin-Based Parabolic Reflector for Spaceborne SAR Antenna. *Int. J. Aeronaut. Space Sci.* **2021**, *22*, 433–444. [CrossRef]
36. Kwon, S.-C.; Jo, M.-S.; Oh, H.-U. Experimental Validation of Fly-Wheel Passive Launch and On-Orbit Vibration Isolation System by Using a Superelastic SMA Mesh Washer Isolator. *Int. J. Aerosp. Eng.* **2017**, *2017*, 1–16. [CrossRef]

-
37. Capece, P. Active SAR Antennas: Design, Development, and Current Programs. *Int. J. Antennas Propag.* **2009**, *2009*, 1–11. [[CrossRef](#)]
 38. Available online: <http://www.nasa.gov> (accessed on 25 March 2021).